Letter

Moiré Kanamori-Hubbard model for transition metal dichalcogenide homobilayers

Nitin Kaushal [1] and Elbio Dagotto[1,2]

[1]*Materials Science and Technology Division, Oak Ridge National Laboratory, Oak Ridge, Tennessee 37831, USA*
[2]*Department of Physics and Astronomy, The University of Tennessee, Knoxville, Tennessee 37996, USA*

Ab initio and continuum model studies predicted that the Γ valley transition metal dichalcogenide (TMD) homobilayers could simulate the conventional multiorbital Hubbard model on the moiré honeycomb lattice. Here, we perform the Wannierization starting from the continuum model and show that a more general moiré Kanamori-Hubbard model emerges, beyond the extensively studied standard multiorbital Hubbard model, which can be used to investigate the many-body physics in the Γ valley TMD homobilayers. Using the unrestricted Hartree-Fock and Lanczos techniques, we study these half-filled multiorbital moiré bands. By constructing the phase diagrams we predict the presence of an antiferromagnetic state and in addition we found unexpected and dominant states, such as a $S = 1$ ferromagnetic insulator and a charge density wave state. Our theoretical predictions made using this model can be tested in future experiments on the Γ valley TMD homobilayers.

Introduction. Transition metal dichalgenide (TMD) moiré materials provide unprecedented platforms to study the effect of electronic correlations on flat moiré bands [1–5]. A variety of low-energy Hamiltonians can be realized in these TMD moiré materials [6]. For example, the WSe_2/WS_2 heterobilayer simulates the one-orbital triangular lattice Hubbard model [7–10], while the AB-stacked $MoTe_2/WSe_2$ leads to nontrivial moiré bands demonstrating quantum anomalous Hall effect [11]. In addition, recent *ab initio* and continuum model calculations have shown that twisted Γ-valley homobilayers, such as MoS_2, $MoSe_2$, and WS_2, produce two valence moiré bands with Dirac cone mimicking a honeycomb lattice, while the next set of lower energy four moiré bands simulates the two-orbital asymmetric p_x-p_y honeycomb lattice model [12–16]. Moreover, surprisingly in recent ARPES experiments Γ-valley moiré bands have been observed in the twisted WSe_2 [17,18], rendering it also a candidate material to realize the two-orbital honeycomb lattice model. These findings opens up an exciting avenue to simulate multiorbital Hubbard-like models in TMD moiré materials.

The Kanamori-Hubbard (KH) model [19,20] has been extensively studied for many conventional materials where multiple orbitals are active, as in iron based superconductors, iridates, manganites, etc. [20–24]. The moiré potential is shallower than the ionic potential present in conventional materials, leading to relatively broader Wannier functions in moiré materials and making nonlocal correlations important [25], which are typically ignored in the often used KH model. This suggests that the theoretical studies of twisted Γ-valley homobilayers require a model going beyond the standard KH model. In this publication, for the first time we provide a moiré Kanamori-Hubbard (mKH) model which includes nonlocal correlations, where the interaction parameters are calculated using the well-localized and accurate Wannier functions of the twisted MoS_2 bilayer [27–29]. The importance of the mKH model is depicted by discussing the effective dielectric

constant ϵ vs the twist angle θ phase diagrams for the half-filled mKH model, unveiling surprising results which definitely cannot be captured by the standard KH model. It is interesting to note that the relevance of the nonlocal correlations in the flat moiré bands of twisted bilayer graphene (TBG) has also been discussed [30–33], so we believe the mKH model can also be used for TBG, but only near magic angles [34–37] unlike in TMD bilayers where the flat bands are present in a larger range of twist angles.

Wannierization and tight-binding model. We calculate the moiré bands structure and the Bloch states using the continuum moiré Hamiltonian $H = -\hbar k^2/2m^* + \Delta(\mathbf{r})$. The moiré potential $\Delta(\mathbf{r})$ is defined as $\Delta(\mathbf{r}) = \sum_s \sum_{j=1}^6 V_s e^{i(\mathbf{g}_j^s \cdot \mathbf{r} + \phi_s)}$, where $\mathbf{g}_j^s$ are the moiré reciprocal lattice vectors connecting to sth nearest neighbor. The model parameters $\{V_s, \phi_s\}$ are fixed following earlier studies [12], considering the MoS_2 homobilayer, so that the band structure obtained from continuum model and *ab initio* matches very well. All of our predictions are also valid for other Γ valley homobilayers like $MoSe_2$ and WS_2. The valence bands closest to the chemical potential can be described by a one-orbital tight-binding model on a honeycomb lattice, see [12,13]. Here, we focus on the second set of four composite valence bands, which can be described by a two-orbital p_x-p_y tight-binding model on the honeycomb lattice. Until now, the Wannier functions have not been calculated for these set of bands. We perform Wannierization, using a projection technique [38,39], to obtain four well-localized Wannier functions, two on each sublattice, namely A and B, see Fig. 1(k) (for details see the Supplemental Material [40]). The calculated Wannier fuctions have nodes at the moiré sites and a pair of lobes like in the p orbitals of the hydrogen atom, as shown in Figs. 1(c)–1(f) and Figs. 1(g)–1(j) for twist angles $1°$ and $2.5°$, respectively. We noticed that $\Psi_{A(B)p_x}(\mathbf{r})$ cannot be obtained by a 90° rotation of $\Psi_{A(B)p_y}(\mathbf{r})$ unlike in the ideal p_x-p_y orbitals, which follows from the absence of full rotational symmetry in the moiré potential. Moreover, we found $\Psi_{Bp_{x(y)}}(\mathbf{r}) = -\Psi_{Ap_{x(y)}}(-\mathbf{r})$ due to the inversion symmetry of
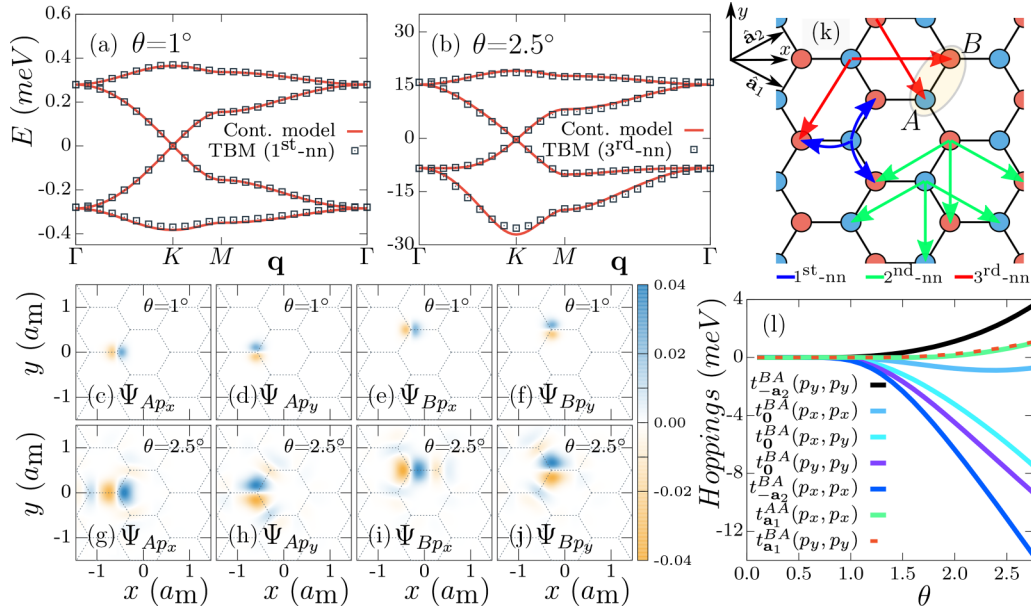
FIG. 1. (a), (b) Comparison between independently calculated band structures using the continuum model and the tight-binding model (TBM), for the twist angles (a) $\theta = 1°$ and (b) $\theta = 2.5°$. Wannier functions, calculated using the continuum model Bloch wavefunctions, for twist angles $\theta = 1°$ and $\theta = 2.5°$ are shown in panels (c)–(f) and (g)–(j), respectively. (k) The honeycomb lattice geometry used in the tight-binding model. The blue, green, and red arrows depicts the nearest, second-nearest, and third-nearest neighbor hoppings, respectively. (l) Evolution of the dominant hopping parameters with the twist angle.

the moiré potential on two sublattices given by $\Delta(\mathbf{r} - \mathbf{R}_A) = \Delta(-\mathbf{r} - \mathbf{R}_B)$.

Using the above Wannier functions, we calculated the hopping parameters for the two-orbital tight-binding model on the honeycomb lattice, up to the third nearest-neighbor using $t_{\mathbf{j}-\mathbf{i}}^{SS'}(\mu, \nu) = \langle \Psi_{S\mu}^{\mathbf{j}} | H | \Psi_{S'\nu}^{\mathbf{i}} \rangle$ (for details see Supplemental Material [40]), where the $\{\mathbf{i}, \mathbf{j}\}$, $\{S, S'\}$, and $\{\mu, \nu\}$ indices denotes unitcell, sublattice, and orbitals (p_x or p_y), respectively. We write the kinetic energy as $H_{\text{K.E.}} = \sum_{\mathbf{i}\sigma} K_{\mathbf{i}\sigma}^1 + K_{\mathbf{i}\sigma}^2 + K_{\mathbf{i}\sigma}^3$, where the terms $K_{\mathbf{i}\sigma}^n$ consists of hoppings between the nth nearest neighbor sites in the honeycomb lattice. The hopping connections up to the third nearest-neighbor are pictorially shown in Fig. 1(k). $K_{\mathbf{i}\sigma}^1$ is presented below:

$$K_{\mathbf{i}\sigma}^1 = \sum_{\substack{\nu, \mu \in \{p_x, p_y\} \\ \mathbf{r} \in \{0, -\mathbf{a}_2, \mathbf{a}_1 - \mathbf{a}_2\}}} t_{\mathbf{r}}^{BA}(\mu, \nu) c_{\mathbf{i}+\mathbf{r}B_\mu \sigma}^\dagger c_{\mathbf{i}A_\nu \sigma} + \text{H.c.} \quad (1)$$

The $K_{\mathbf{i}\sigma}^{2(3)}$ terms can be written similarly, as shown in the Supplemental Material [40]. The first nearest-neighbor hopping term $K_{\mathbf{i}\sigma}^1$, shown in Eq. (1), depends on three 2×2 matrices, namely $\{t_0^{BA}, t_{-\mathbf{a}_2}^{BA}, t_{\mathbf{a}_1-\mathbf{a}_2}^{BA}\}$. Similarly, six 2×2 matrices $\{t_{\mathbf{a}_1}^{AA}, t_{-\mathbf{a}_2}^{AA}, t_{\mathbf{a}_1-\mathbf{a}_2}^{AA}, t_{\mathbf{a}_1}^{BB}, t_{-\mathbf{a}_2}^{BB}, t_{\mathbf{a}_1-\mathbf{a}_2}^{BB}\}$ and three 2×2 matrices $\{t_{\mathbf{a}_1}^{AB}, t_{\mathbf{a}_1}^{BA}, t_{\mathbf{a}_1-2\mathbf{a}_2}^{BA}\}$ are required for the second and third nearest-neighbor hoppings, respectively. All of these 12 matrices are dependent on θ. We found a good match between the band-structure calculated using the above tight-binding model and the continuum model, as shown in Figs. 1(a) and 1(b), suggesting that we have accurate Wannier functions. We noticed that for $\theta \lesssim 1.2$, only nearest-neighbor hoppings are enough to obtain the correct bandstructure, as shown in Fig. 1(a) for $\theta = 1.0$. However, for larger θ longer-range hoppings are required to reproduce the continuum model results

[see Fig. 1(b), for $\theta = 2.5$]. We show the evolution of the some dominant hopping parameters in Fig. 1(l), depicting the exponential fast growth of hoppings with θ.

Interaction parameters and moiré Kanamori-Hubbard model. Now we will derive the Coulomb interaction between the fermions in the Wannier states discussed above. The generic interaction term can be written as

$$H_{\text{Int}} = 1/2 \sum_{\substack{\mathbf{i}, \mathbf{j}, \mathbf{k}, \mathbf{l}, \\ \alpha, \beta, \gamma, \delta, \\ \sigma, \sigma'}} V_{\mathbf{ijkl}}^{\alpha\beta\gamma\delta} c_{\mathbf{i}\alpha\sigma}^\dagger c_{\mathbf{j}\beta\sigma'}^\dagger c_{\mathbf{l}\delta\sigma'} c_{\mathbf{k}\gamma\sigma}, \quad (2)$$

where $V_{\mathbf{ijkl}}^{\alpha\beta\gamma\delta} = \langle \Psi_\alpha^{\mathbf{i}} \Psi_\beta^{\mathbf{j}} | V | \Psi_\gamma^{\mathbf{k}} \Psi_\delta^{\mathbf{l}} \rangle$ and $V = e^2/\epsilon |\mathbf{r}_1 - \mathbf{r}_2|$. ϵ is produced by the surrounding dielectric environment, such as nearby h-BN layers. The exact value of ϵ is not known so we keep it as a free parameter. The $\{\alpha, \beta, \gamma, \delta\}$ indices represent the sublattice S and the orbital μ via $\alpha = 2S + \mu = S_\mu$, where the sublattice $A(B) = 0(1)$ and the orbital $p_x(p_y) = 0(1)$.

In the present work, for simplicity, we limit the nonlocal Coulomb interactions only up to nearest-neighbor sites of the honeycomb lattice. *A priori*, the longer range interactions are not expected to be very relevant at and near half-filling [41]. To study Wigner crystals at fractional fillings, the approximate longer range interactions can be easily included by assuming the $(\frac{1}{|r|} - \frac{1}{\sqrt{r^2+d^2}})$ functional form, where d is the screening length [42–44]. The Coulomb interaction term which includes up to nearest-neighbour interactions can be divided into three parts, $H_{\text{Int}} = \sum_{\mathbf{i}} H_{\mathbf{i}} + H_{\mathbf{i},\mathbf{i}-\mathbf{a}_2}^{AB} + H_{\mathbf{i},\mathbf{i}+\mathbf{a}_1-\mathbf{a}_2}^{AB}$, where $\mathbf{i}$ is the unit cell index and $\mathbf{a}_{(1,2)}$ are the Bravais lattice vectors. The first part $H_{\mathbf{i}}$ consists of all the Coulomb interactions possible within the unit cell $\mathbf{i}$, including both local and nearest-neighbor interactions given by $V_{\mathbf{iiii}}^{\alpha\beta\gamma\delta}$ (total 4^4 terms). The second $H_{\mathbf{i},\mathbf{i}-\mathbf{a}_2}^{AB}$ and third parts $H_{\mathbf{i},\mathbf{i}+\mathbf{a}_1-\mathbf{a}_2}^{AB}$ contain

the Coulomb interactions between the nearest-neighbor sites belonging to different unit cells. Now we will discuss the $H_{\mathbf{i}}$ term in detail; the other two terms are very similar and shown in the Supplemental Material. $H_{\mathbf{i}}$ is shown in Eq. (3), where $\mathbf{S}_{\mathbf{i}\alpha} = \frac{1}{2}\sum_{s,s'} c^{\dagger}_{\mathbf{i}\alpha s}\boldsymbol{\tau}_{ss'}c_{\mathbf{i}\alpha s'}$ represent the spin at unit cell $\mathbf{i}$, orbital $\mu = \mathrm{mod}(\alpha, 2)$, and sublattice $= (\alpha - \mu)/2$. The pair annihilation operator is defined as $P_{\mathbf{i}\alpha} = c_{\mathbf{i}\alpha\downarrow}c_{\mathbf{i}\alpha\uparrow}$. $s = 1(-1)$ for $\sigma = \uparrow (\downarrow)$, and the set $\mathbb{S} = \{\{0123\}, \{0132\}, \{0213\}\}$.

$$
\begin{aligned}
H_{\mathbf{i}} = {} & U_0 \sum_{\alpha} n_{\mathbf{i}\alpha\uparrow} n_{\mathbf{i}\alpha\downarrow} + \sum_{\alpha<\beta}\left(U_{\alpha\beta} - \frac{J_{\alpha\beta}}{2}\right)n_{\mathbf{i}\alpha}n_{\mathbf{i}\beta} \\
& - 2\sum_{\alpha<\beta} J_{\alpha\beta}\mathbf{S}_{\mathbf{i}\alpha}\cdot\mathbf{S}_{\mathbf{i}\beta} + \sum_{\alpha<\beta} J_{\alpha\beta}(P^{\dagger}_{\mathbf{i}\alpha}P_{\mathbf{i}\beta} + \mathrm{H.c.}) \\
& + 1/2 \sum_{\sigma,\sigma',\alpha\neq\beta\neq\gamma}(A_{\beta\alpha\gamma} - \delta_{\sigma\sigma'}\tilde{J}_{\beta\alpha\gamma})(c^{\dagger}_{\mathbf{i}\alpha\sigma}c_{\mathbf{i}\gamma\sigma}n_{\mathbf{i}\beta,\sigma'} + \mathrm{H.c.}) \\
& + \sum_{\sigma,\alpha\neq\beta}\tilde{A}_{\alpha\beta}(c^{\dagger}_{\mathbf{i}\alpha\sigma}c_{\mathbf{i}\beta\sigma}n_{\mathbf{i}\beta\bar{\sigma}} + \mathrm{H.c.}) \\
& - \sum_{\alpha\neq\beta\neq\gamma}\tilde{J}_{\alpha\gamma\beta}(S^{+}_{\mathbf{i}\alpha}c^{\dagger}_{\mathbf{i}\beta\downarrow}c_{\mathbf{i}\gamma\uparrow} + \mathrm{H.c.}) \\
& + 1/2 \sum_{\sigma,\alpha\neq\beta\neq\gamma}\tilde{J}_{\alpha\gamma\beta}s(P^{\dagger}_{\mathbf{i}\alpha}c_{\mathbf{i}\gamma\bar{\sigma}}c_{\mathbf{i}\beta\sigma} + \mathrm{H.c.}) \\
& + \sum_{\substack{\sigma,\sigma',\\\{\alpha\beta\gamma\delta\}\in\mathbb{S}}}T_{\alpha\beta\gamma\delta}(c^{\dagger}_{\mathbf{i}\alpha\sigma}c_{\mathbf{i}\gamma\sigma}(c^{\dagger}_{\mathbf{i}\beta\sigma'}c_{\mathbf{i}\delta\sigma'} + c^{\dagger}_{\mathbf{i}\delta\sigma'}c_{\mathbf{i}\beta\sigma'}) + \mathrm{H.c.}).
\end{aligned}
$$

$$(3)$$

Equation (3) encompasses all 4^4 intraunit cell interaction terms. The first four terms look similar to the conventional multiorbital Hubbard model, but here they capture the nonlocal interactions as well.

The first term is the standard onsite intraorbital Hubbard repulsion, where $U_0 = V^{\alpha\alpha\alpha\alpha}_{\mathbf{iiii}}$ (same for all α's). The second term incorporates the onsite interorbital density-density repulsions via parameters $\{U_{01}, U_{23}, J_{01}, J_{23}\}$ and the nonlocal orbital resolved repulsions via parameters like U_{02}, J_{02}, etc., where $U_{\alpha\beta} = V^{\alpha\beta\alpha\beta}_{\mathbf{iiii}}$ and $J_{\alpha\beta} = V^{\alpha\beta\beta\alpha}_{\mathbf{iiii}}$. The well known local Hund's coupling is present in the third term via the dominant J_{01} and J_{23} parameters; this term also includes the nonlocal ferromagnetic direct exchange terms ($J_{02}, J_{13}, J_{03}, J_{12}$). The fourth term incorporate the onsite interorbital and nonlocal pair hopping terms. We also found interaction assisted hoppings (termfive and termsix), spin-flip hoppings accompanied with local spin flip (termseven), and scattering of doublon to different states (termeight) quantified by ($A_{\beta\alpha\gamma}, \tilde{A}_{\alpha\beta}, \tilde{J}_{\beta\alpha\gamma}$). The remaining interactions are present in term nine.

We show the interaction parameters of the first six terms as a function of θ in Fig. 2. The density-density terms are dominant interactions, see Fig. 2(a). The onsite intraorbital repulsion (U_0) suggests that $\epsilon U_0/W$ can be of order of 10 to 1000 in real materials, depending on θ, where W is the noninteracting bandwidth. For example, U_0/W is about $1200\epsilon^{-1}$ and $25\epsilon^{-1}$ for $\theta = 1°$ and $\theta = 2.5°$, respectively. The local Hund's coupling and the nonlocal ferromagnetic direct exchange is shown in Fig. 2(b). Figures 2(c) and 2(d) display the interaction assisted hoppings vs θ. The rest of the interaction
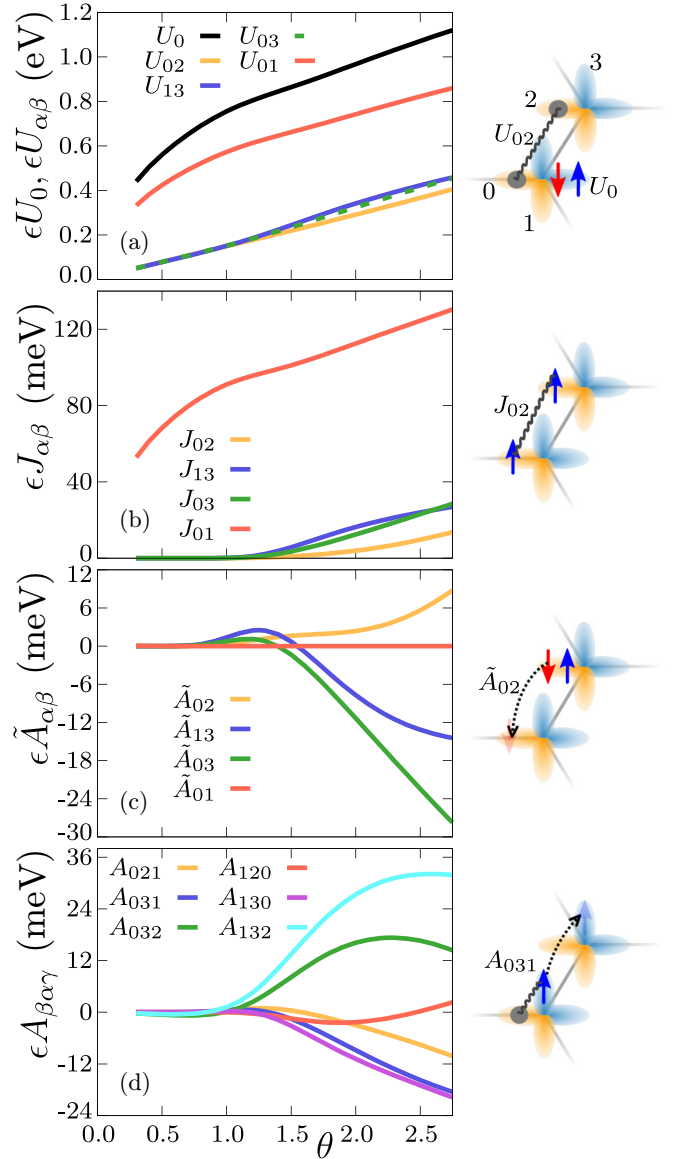
FIG. 2. (a) The onsite intraorbital Hubbard repulsion U_0, onsite interorbital Hubbard repulsion U_{01}, and the orbital resolved nearest-neighbor Hubbard repulsion parameters $\{U_{02}, U_{03}, U_{13}\}$ shown for various twist angle θ values. (b) The onsite Hund's coupling J_{01} and the orbital resolved nearest neighbor direct-exchange parameters $\{J_{02}, J_{03}, J_{13}\}$ as a function of θ. (c), (d) Evolution of nearest-neighbor interaction assisted hoppings with θ, requiring electron pair in the sameorbital (c) or on the samesite (d). ϵ is the effective dielectric constant.

parameters are relatively smaller, and shown in the Supplemental Material. We call the total Hamiltonian $H = H_{\mathrm{K.E.}} + H_{\mathrm{Int}}$ the moiré Kanamori-Hubbard model because of the presence of nonlocal interaction terms, which are ignored in the standard KH model. These nonlocal correlations can lead to unexpected results, as shown in the next section. It should be noted that the mKH model shown here has larger scope and can also be used for magic-angle TBG and future moiré materials addressing multiorbital physics on honeycomb lattice (only the values of hopping and interaction parameters will depend on the specific material).
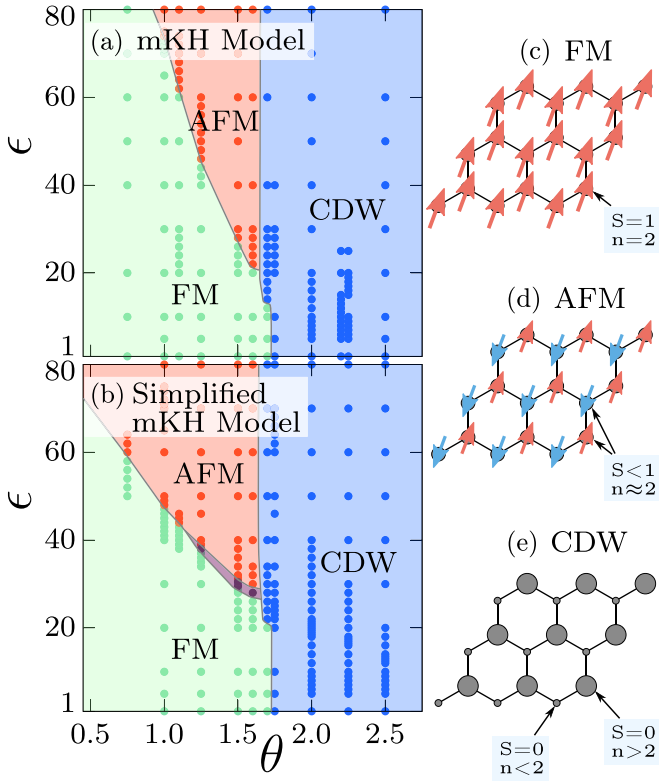
FIG. 3. (a), (b) Effective dielectric constant ϵ vs twist angle θ phase diagrams for (a) the full moiré Kanamori-Hubbard (mKH) model and (b) the simplified mKH model, both constructed via unrestricted Hartree-Fock. Panels (c), (d), and (e) show the pictorial representation of ferromagnetic (FM), antiferromagnetic (AFM), and charge density wave (CDW) states, respectively. The tiny violet regions in (b) correspond to noncollinear and noncoplanar phases.

In recent theoretical work [25], a one-orbital Hubbard model with nonlocal interactions was derived for TMD heterobilayers. As discussed before, in our work we instead derive a *multi-orbital* Hubbard model, focusing on homobilayers. We found similar nonlocal interactions terms as discussed in [25], such as density-density repulsion, ferromagnetic direct exchange, interaction-assisted hopping, and pairhopping. However, in addition we also found spin-flip hoppings assisted by local spinflip, and doublon scattering to different sites. Moreover, the orbital degree of freedom in our model may lead to phenomena unique of multiorbital models, such as orbital ordering [26], local Hund's coupling driven double-exchange mechanisms [20], etc.

Numerical results at half-filling. We create ϵ vs θ phase diagrams to investigate the physics of the mKH model at half-filling $n = N/L = 2$, where N is the total number of fermions and $L = L_1 \times L_2$ the total number of unit cells. We studied 6×6 and 12×12 system sizes using the unrestricted Hartree-Fock technique. We choose a broad range of $\epsilon \in [1, 80]$ as it can be tuned by changing the distance with the nearby metallic gate. Moreover, ϵ will be enhanced by the charge fluctuations between the moiré bands considered here and other remote moiré bands. The ϵ vs θ phase diagram for the mKH model is shown in Fig. 3(a). In addition to the expected antiferromagnetic (AFM) state, we have unveiled two states not anticipated
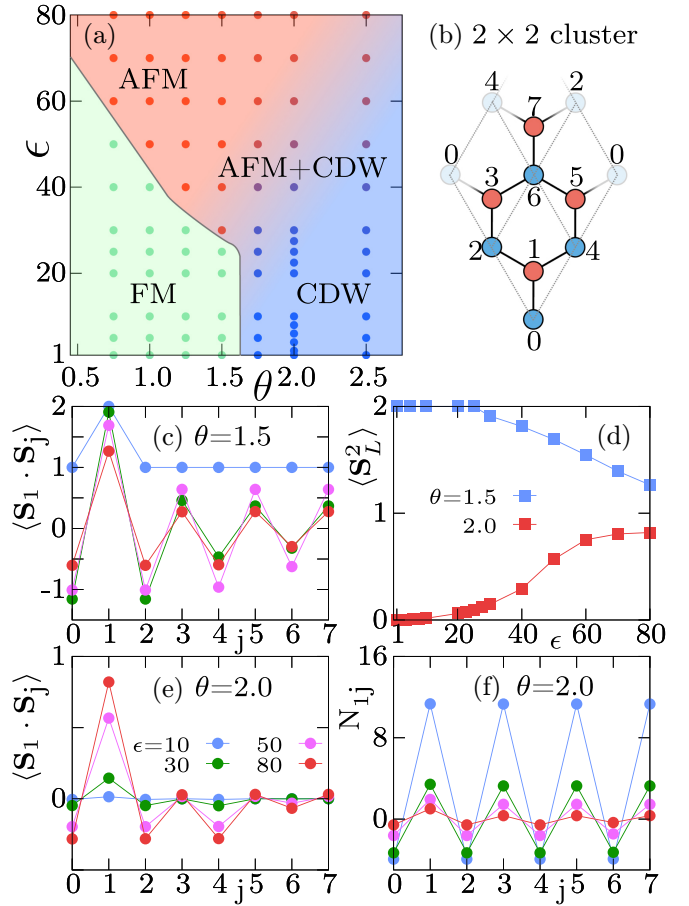
FIG. 4. (a) Effective dielectric constant ϵ vs twist angle θ phase diagram for the simplified mKH model by solving the small 2×2 cluster using the Lanczos technique. The 2×2 honeycomb cluster with periodic boundary conditions is shown in (b); the dashed thin lines depicts the underlying triangular Bravais lattice. (c), (e) The spin-spin correlation with respect to site=1 ($\langle \mathbf{S}_1 \cdot \mathbf{S}_j \rangle$) for various values of ϵ, at fixed (c) $\theta = 1.5$ and (e) $\theta = 2.0$. (d) The local moment $\langle \mathbf{S}_L^2 \rangle$ for $\theta = 1.5$ and 2.5 vs. ϵ. (f) The density-density correlation with respect to site=1 (N_{1j}) for various values of ϵ, at fixed $\theta = 2.0$.

to be stable in the conventional multiorbital model: the $S = 1$ ferromagnetic (FM) state for $\theta < 1.75$ and the charge density wave (CDW) state for $\theta \geqslant 1.75$. The nonlocal density-density repulsion plays the key role to stabilize the CDW state. We can estimate the nearest-neighbor density-density repulsion to onsite intraorbital repulsion ratio. For example, U_{02}/U_0 lies approximately in the range [0.20, 0.35] for the homobilayer we considered, whereas for heterobilayer the nearest-neighbor density repulsion to onsite Hubbard repulsion ratio lies in [0.12, 0.25] [25]. Although our estimates are in a similar range, the half-filled heterobilayer does not show the CDW state [25], whereas our multiorbital mKH model shows CDW in a large region of the phase diagram. This can be understood by the approximate CDW stability condition for our model which incorporates multiple orbitals and enhances the effect of nonlocal correlations, i.e., $2(U_{01} + U_0) < 3(U_{02} + U_{03} + U_{12} + U_{13})$ which is satisfied for $\theta \gtrsim 1.75$. The competition between the nonlocal FM direct exchange ($\propto \epsilon^{-1}(J_{02} + J_{13} + 2J_{03})$)

and the AFM superexchange ($\propto (\epsilon t^2)/(U_0 + J_{01})$) leads to the transition from the FM to AFM state as ϵ increases. We found that the AFM state is present only for $\epsilon > 20$ with local moment S < 1. See Figs. 3(c), 3(d), and 3(e) for the pictorial representation of the FM, AFM, and CDW states.

We also used the simplified mKH model, only keeping the first four terms in Eq. (3), and found all three phases are present nearly in the same region of the phase diagram [see Fig. 3(b)], suggesting that the FM direct exchange and the density-density repulsion are the most important nonlocal interactions for the half-filled mKH model.

To investigate the effect of the quantum fluctuations, we used the Lanczos technique and studied a small 2×2 cluster with periodic boundary conditions [Fig. 4(b)], using the simplified mKH model. The phase diagram is shown in Fig. 4(a). We again found the FM, AFM, and CDW states in the same region of the phase diagram. Figure 4(c) shows the spin-spin correlation, with respect to site=1, $\langle \mathbf{S}_1 \cdot \mathbf{S}_j \rangle$ for $\theta = 1.5°$, depicting strong FM correlations for $\epsilon = 10$, and AFM correlations for $\epsilon \in \{30, 50, 80\}$. Figures 4(e) and 4(f) show $\langle \mathbf{S}_1 \cdot \mathbf{S}_j \rangle$ and density-density correlations $N_{1j} = \langle n_1 n_j \rangle - \langle n_1 \rangle \langle n_j \rangle$, respectively, at fixed $\theta = 2.0$ depicting the growth of AFM correlations and suppression in the CDW as ϵ increases. This indicates a smooth transition from the CDW phase to the AFM phase. We believe larger systems are required to confirm whether it is a second-order phase transition or a crossover. The FM to AFM or the FM to CDW are first order transitions because the total spin suddenly changes from $2L = 8$ to 0. The averaged local moment $\mathbf{S}_L^2 = (1/4L) \sum_{i\alpha} \langle \mathbf{S}_{i\alpha}^2 \rangle$ as a function of ϵ is shown in Fig. 4(d). We found, for $\theta < 1.75$, that $\mathbf{S}_L^2$ decreases as ϵ is increased while the system transits from the S=1 FM to AFM phases, whereas for $\theta \geqslant 1.75$,

$\mathbf{S}_L^2$ grows with ϵ developing AFM correlations with weak CDW.

We have focused only on half-filling but investigating other fillings would also be valuable, because including longer-range interactions will likely lead to rich and novel multiorbital phase diagrams at fractional fillings [45–47]. Our model provides a unique platform to explore the interplay between multiorbital interactions and nonlocal correlations. Deriving the low energy S=1 model for half-filling [48] and the $t - J$ model for theoretical studies near half-filling can also be interesting future directions, as the TMD moiré materials are generally located in the strong coupling regime.

Conclusions. We showed that the twisted Γ-valley TMD bilayers contains physics beyond the conventional multiorbital Hubbard model. We provide a mKH model which can be used to theoretically study the multiorbital physics of TMD bilayers. Using our numerical studies at half-filled moiré bands we show that the nonlocal direct-exchange terms and density-density interactions can lead to S=1 FM insulators and CDW states, respectively, depending on ϵ and θ. The AFM state can also be obtained but at large $\epsilon > 20$. Our theoretical prediction of a S=1 FM insulator can be verified by measuring the magnetic susceptibility and Weiss constant in real materials [7,49], and the charge ordered state can be observed using high-resolution scanning tunneling experiments [50]. The mKH model can also be used for further theoretical investigations like doping near half-filled correlated insulators and for studying Mott-Wigner crystals at fractional fillings by including longer range density-density interactions.

[1] K. F. Mak and J. Shan, Nat. Nanotechnol. **17**, 686 (2022).

[2] C. Zhang, C.-P. Chuu, X. Ren, M. Y. Li, L. J. Li, C. Jin, M. Y. Chou, and C. K. Shih, Sci. Adv. **3**, e1601459 (2017).

[3] Y. Pan, S. Fölsch, Y. Nie, D. Waters, Y.-C. Lin, B. Jariwala, K. Zhang, K. Cho, J. A. Robinson, and R. M. Feenstra, Nano Lett. **18**, 1849 (2018).

[4] L. J. McGilly, A. Kerelsky, N. R. Finney, K. Shapovalov, E.-M. Shih, A. Ghiotto, Y. Zeng, S. L. Moore, W. Wu, Y. Bai, K. Watanabe, T. Taniguchi, M. Stengel, L. Zhou, J. Hone, X. Zhu, D. N. Basov, C. Dean, C. E. Dreyer, and A. N. Pasupathy, Nat. Nanotechnol. **15**, 580 (2020).

[5] E. Y. Andrei, D. K. Efetov, P. Jarillo-Herrero, A. H. MacDonald, K. F. Mak, T. Senthil, E. Tutuc, A. Yazdani, and A. F. Young, Nat. Rev. Mater. **6**, 201 (2021).

[6] D. M. Kennes, M. Claassen, L. Xian, A. Georges, A. J. Millis, J. Hone, C. R. Dean, D. N. Basov, A. N. Pasupathy, and A. Rubio, Nat. Phys. **17**, 155 (2021).

[7] Y. Tang, L. Li, T. Li, Y. Xu, S. Liu, K. Barmak, K. Watanabe, T. Taniguchi, A. H. MacDonald, J. Shan, and K. F. Mak, Nature (London) **579**, 353 (2020).

[8] E. C. Regan, D. Wang, C. Jin, M. I. B. Utama, B. Gao, X. Wei, S. Zhao, W. Zhao, Z. Zhang, K. Yumigeta, M. Blei, J. D. Carlström, K. Watanabe, T. Taniguchi, S. Tongay, M. Crommie, A. Zettl, and F. Wang, Nature (London) **579** 359 (2020).

[9] C. Jin, E. C. Regan, A. Yan, M. I. B. Utama, D. Wang, S. Zhao, Y. Qin, S. Yang, Z. Zheng, S. Shi, K. Watanabe, T. Taniguchi, S. Tongay, A. Zettl, and F. Wang, Nature (London) **567**, 76 (2019).

[10] F. Wu, T. Lovorn, E. Tutuc, and A. H. MacDonald, Phys. Rev. Lett. **121**, 026402 (2018).

[11] T. Li, S. Jiang, B. Shen, Y. Zhang, L. Li, Z. Tao, T. Devakul, K. Watanabe, T. Taniguchi, L. Fu, J. Shan, and K. F. Mak, Nature (London) **600**, 641 (2021).

[12] M. Angeli and A. H. MacDonald, Proc. Natl. Acad. Sci. USA **118**, e2021826118 (2021).

[13] L. Xian, M. Claassen, D. Kiese, M. M. Scherer, S. Trebst, D. M. Kennes, and A. Rubio, Nat. Commun. **12**, 5644 (2021).

[14] V. Vitale, K. Atalar, A. A. Mostofi, and J. Lischner, 2D Mater. **8**, 045010 (2021).

[15] N. Witt, J. M. Pizarro, J. Berges, T. Nomoto, R. Arita, and T. O. Wehling, Phys. Rev. B **105**, L241109 (2022).

[16] C. Wu, D. Bergman, L. Balents, and S. Das Sarma, Phys. Rev. Lett. **99**, 070401 (2007).

[17] D. Pei, B. Wang, Z. Zhou, Z. He, L. An, S. He, C. Chen, Y. Li, L. Wei, A. Liang *et al.*, Phys. Rev. X **12**, 021065 (2022).

[18] G. Gatti, J. Issing, L. Rademaker, F. Margot, T. A. de Jong, S. J. van der Molen, J. Teyssier, T. K. Kim, M. D. Watson, C. Cacho, *et al.*, arXiv:2211.01192.

[19] J. Kanamori, Prog. Theor. Phys. **30**, 275 (1963).

[20] E. Dagotto, T. Hotta, and A. Moreo, Phys. Rep. **344**, 1 (2001).

[21] J. Herbrych, N. Kaushal, A. Nocera, G. Alvarez, A. Moreo, and E. Dagotto, Nat. Commun. **9**, 3736 (2018).

[22] J. Herbrych, J. Heverhagen, N. D. Patel, G. Alvarez, M. Daghofer, A. Moreo, and E. Dagotto, Phys. Rev. Lett. **123**, 027203 (2019).

[23] N. Kaushal, J. Herbrych, A. Nocera, G. Alvarez, A. Moreo, F. A. Reboredo, and E. Dagotto, Phys. Rev. B **96**, 155111 (2017).

[24] B. J. Kim, Hosub Jin, S. J. Moon, J.-Y. Kim, B.-G. Park, C. S. Leem, Jaejun Yu, T. W. Noh, C. Kim, S.-J. Oh, J.-H. Park, V. Durairaj, G. Cao, and E. Rotenberg, Phys. Rev. Lett. **101**, 076402 (2008).

[25] N. M. Morales-Durán, N. C. Hu, P. Potasz, and A. H. MacDonald, Phys. Rev. Lett. **128**, 217202 (2022).

[26] L.-F. Lin, N. Kaushal, Y. Zhang, A. Moreo, and E. Dagotto, Phys. Rev. Mater. **5**, 025001 (2021).

[27] M. H. Naik and M. Jain, Phys. Rev. Lett. **121**, 266401 (2018).

[28] M. H. Naik, S. Kundu, I. Maity, and M. Jain, Phys. Rev. B **102**, 075413 (2020).

[29] M. Liao, Z. Wei, L. Du, Q. Wang, J. Tang, H. Yu, F. Wu, J. Zhao, X. Xu, B. Han, K. Liu, P. Gao, T. Polcar, Z. Sun, D. Shi, R. Yang, and G. Zhang, Nat. Commun. **11**, 2153 (2020).

[30] N. F. Q. Yuan and L. Fu, Phys. Rev. B **98**, 045103 (2018).

[31] M. Koshino, N. F. Q. Yuan, T. Koretsune, M. Ochi, K. Kuroki, and L. Fu, Phys. Rev. X **8**, 031087 (2018).

[32] J. Kang and O. Vafek, Phys. Rev. X **8**, 031088 (2018).

[33] B. Andrews and A. Soluyanov, Phys. Rev. B **101**, 235312 (2020).

[34] R. Bistritzer and A. H. MacDonald, Proc. Natl. Acad. Sci. USA **108**, 12233 (2011).

[35] Y. Cao, V. Fatemi, S. Fang, K. Watanabe, T. Taniguchi, E. Kaxiras, and P. Jarillo-Herrero, Nature (London) **556**, 43 (2018).

[36] Y. Cao, V. Fatemi, A. Demir, S. Fang, S. L. Tomarken, J. Y. Luo, J. D. Sanchez-Yamagishi, K. Watanabe, T. Taniguchi, E. Kaxiras, R. C. Ashoori, and P. Jarillo-Herrero, Nature (London) **556**, 80 (2018).

[37] E. Y. Andrei and A. H. MacDonald, Nat. Mater. **19**, 1265 (2020).

[38] N. Marzari, A. A. Mostofi, J. R. Yates, I. Souza, and D. Vanderbilt, Rev. Mod. Phys. **84**, 1419 (2012).

[39] N. Marzari and D. Vanderbilt, Phys. Rev. B **56**, 12847 (1997).

[40] The Supplemental Material can be found at http://link.aps.org/supplemental/10.1103/PhysRevB.107.L201118 for details of (a) the Wannierization procedure, (b) calculations of hopping and interaction parameters, (c) the nearest neighbor interaction terms, and (d) the unrestricted Hartree-Fock technique.

[41] H. Pan and S. Das Sarma, Phys. Rev. Lett. **127**, 096802 (2021).

[42] N. Kaushal, N. Morales-Durán, A. H. MacDonald, and E. Dagotto, Commun. Phys. **5**, 289 (2022).

[43] H. Pan, F. Wu, and S. D. Sarma, Phys. Rev. B **102**, 201104 (2020).

[44] N. Morales-Durán, P. Potasz, and A. H. MacDonald, arXiv:2210.15168.

[45] J. Rincón, A. Moreo, G. Alvarez, and E. Dagotto, Phys. Rev. Lett. **112**, 106405 (2014).

[46] J. Rincón, A. Moreo, G. Alvarez, and E. Dagotto, Phys. Rev. B **90**, 241105(R) (2014).

[47] J. Herbrych, J. Heverhagen, G. Alvarez, and E. Dagotto, Proc. Natl. Acad. Sci. USA **117**, 16226 (2020).

[48] R. Soni, N. Kaushal, C. Şen, F. A. Reboredo, A. Moreo, and E. Dagotto, New J. Phys. **24**, 073014 (2022).

[49] Y. Tang, K. Su, L. Li, Y. Xu, S. Liu, K. Watanabe, T. Taniguchi, J. Hone, C.-M. Jian, C. Xu, K. F. Mak, and J. Shan, Nat. Nanotechnol. **18**, 233 (2023).

[50] H. Li, S. Li, E. C. Regan, D. Wang, W. Zhao, S. Kahn, K. Yumigeta, M. Blei, T. Taniguchi, K. Watanabe, S. Tongay, A. Zettl, M. F. Crommie, and F. Wang, Nature (London) **597**, 650 (2021).